

Chapter 1

Experiment Setup

1.1 Overview

1.1.1 Accelerator

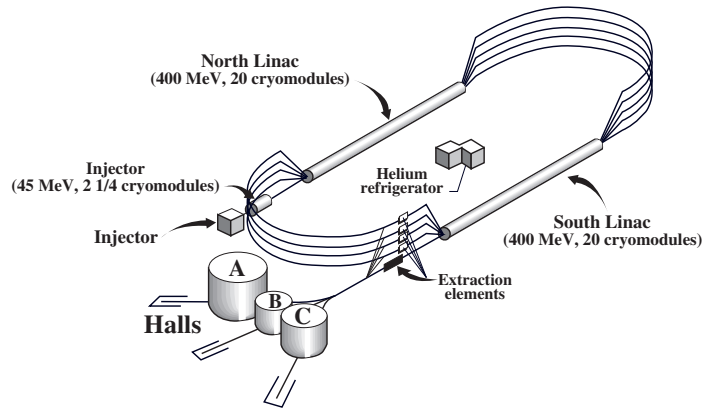


Figure 1.1: The Jefferson Lab Accelerator

Thomas Jefferson Lab (JLab) is a world's leading medium energy electron scattering laboratory, consisting of a continuous electron beam accelerator facility (CEBAF), three experimental halls (A, B and C), a free electron laser facility and several applied research centers (Fig. 1.1). An upgrade project has been proceeding to extend the beam energy from 6 GeV to 12 GeV, and a complete new experimental hall, Hall D,

is currently under construction and expected to start taking data on late 2014.

CEBAF uses the radio frequency (RF) technique to deliver the polarized continuous-wave (CW) electron beam simultaneously to all three experimental halls. An injector provides electrons with the polarization up to 85% and the maximum current of $200 \mu A$. The electron beam gains $400 \sim 600 MeV$ energy when passing through one of two super-conducting linear accelerators (linac), so the energy of the electron can be in the range of $0.8 GeV$ and $6.0 GeV$ within 5 maximum passes. Two arcs connect the linacs and provide 180^0 bending. The electron beam can be delivered into three halls with different energy and current. During E08-014 experiment, an average $3.356 GeV$ electron beam was delivered into Hall A with current up to $150 \mu A$ and the polarization was not required.

1.1.2 Hall-A Overview

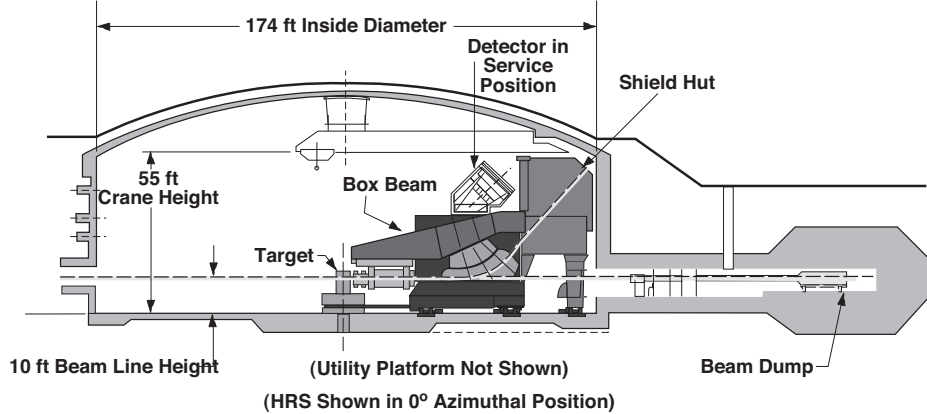


Figure 1.2: Side View of Hall-A

Hall-A is a circular bulk (Fig. 1.2) with a diameter of $53 m$ buried underground with concrete and earth. As shown in Fig. 1.3, the central elements in the hall include beamline components, a target system, and two identical high resolution spectrometers (HRSs). A detector package and the associated front-end electronic modules are stored in a concrete hut, which locates on top of each HRS after the Q3

exit and protects the instruments from any radiation damage. The detector huts also store electronic modules to collect signal outputs from detectors and the beamline, generate triggers, and provide the front end of a CEBAF Online Data Acquisition system (CODA). A detailed discussion of the Hall-A instrumentation is presented in the reference [1].

View of Hall A Machines

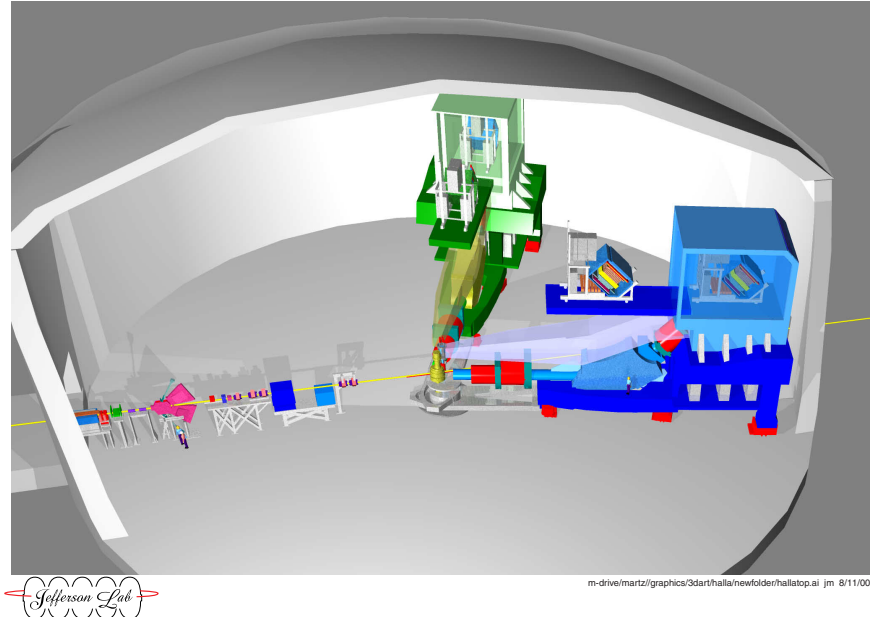


Figure 1.3: Top View of HAll-A

1.2 Beam

Electron beam is delivered into Hall-A through a stainless steel tube which is *10 ft* above the hall floor and can hold a vacuum pressure $\leq 10^{-6}$ *Torr*. The beam optics elements, including quadrupoles, sextupoles and corrector magnets, focus the beam on the target with spot sizes of $100 - 200\mu m$. A raster system located at *23 cm* upstream of the target position provides a larger beam spot over several millimeters at the target. The beam striking through the target is sent into the beam

dump and diffused by a diffuser, consisting of two 6.4 mm thick beryllium foils with water flowing between them. In addition, as showed in Fig. 1.4 [1], there are several beam diagnostics elements along the beamline to monitor, determine and control the relevant properties of the beam, which include the beam current, the electron energy and polarization, the beam position and direction, and the beam spot size at the target location.

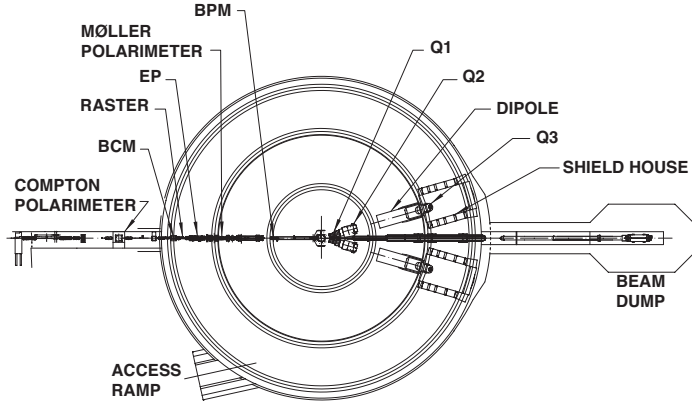


Figure 1.4: Schematic layout of beam instruments and spectrometers in HAll-A, including beamline components, beam diagnostic elements, and beam dump.

1.2.1 Beam Position

The beam position and direction at the target are measured by two beam position monitors (BPMs) located at 7.524 m and 1.286 m upstream of the target. Each BPM contains 4 antennas orientated in different directions inside the beam pipe. Each antenna picks up a voltage reading from the beam with the beam current above 1 μA , and the four signals are used to calculate the beam position within 100 μm of resolution. BMPs have to be calibrated independently to obtain the absolute position of the beam. When taking the calibration data, two pre-surveyed super-harps adjacent to BMPs were used to determine the absolute beam position [2]. Event-by-event information from the BMPs are injected into the data stream, while

the average position over every 0.3 s is also injected into the data stream for every $3 - 4\text{ s}$.

1.2.2 Beam Current and Charge

The beam current monitor (BCM) is installed at 25 m upstream of the target location and provides a non-interfering measurement of beam current. It consists of an Unser monitor, two RF cavities, several electronic modules and an associated DAQ system [1]. Two cavities on either side of the Unser Monitor are high frequency wave-guides, the signal strength of which should be proportional to the value of beam current when they are tuned to the frequency of the beam. Before sending into RMS-to-DC converters, each BCM output signal is split into three copies, two of which are amplified by 3 times and 10 times, respectively. Hence there are totally six digital signals, U_1 , U_3 , U_{10} , D_1 , D_3 and D_{10} , each of which is divided into two copies and fed separately into scalers in HRSs. To obtain total accumulated beam charge from scaler counts in one run, the BCM scalers have to be calibrated using BCM calibration data [3].

1.2.3 Beam Energy

The absolute energy of the beam can be determined by measuring the bend angle of the beam in the arc section of the beamline [4, 5]. The momentum of the beam is related to the field integral of the eight dipoles and the bend angle:

$$p = k \frac{\vec{B} \cdot \vec{dl}}{\theta}, \quad (1.1)$$

where $k = 0.299792\text{ GeV} \cdot \text{rad} \cdot T^{-1} m^{-1} / c$ and θ is the bend angle. The magnetic field integral of the eight dipoles are measured with respect to a reference dipole, the 9th dipole. The value of the bend angle is measured with a set of wire scanners.

There is another method available to provide an secondary beam energy measurement [4,5]. Utilizing a stand-alone device along the beamline located 17 m before the targer, the eP method measures the scattered electrons and protons in the ${}^1H(e, e'p)$ elastic reaction, where the beam energy can be uniquely determined with known scattering angles. Both methods show good agreement within the uncertainties $\leq 3^{-4}$. The beam energy is monitored when taking the data and the values is stored into the data stream.

1.3 Target System

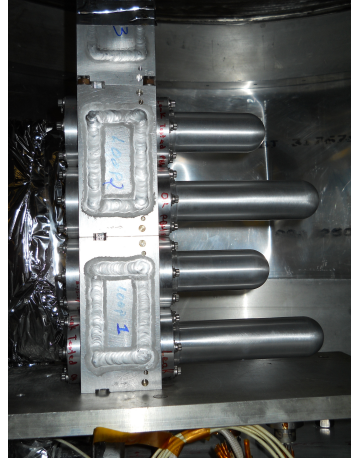
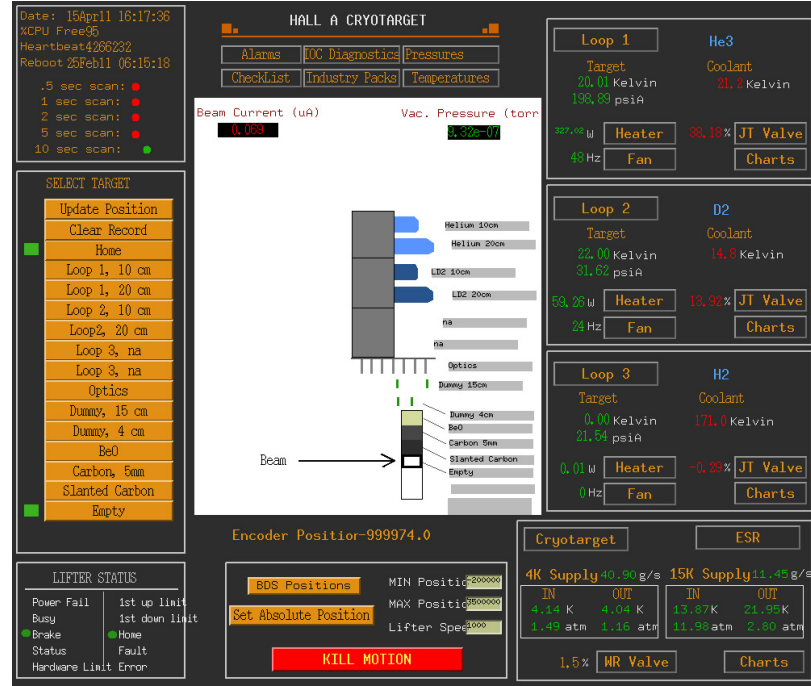


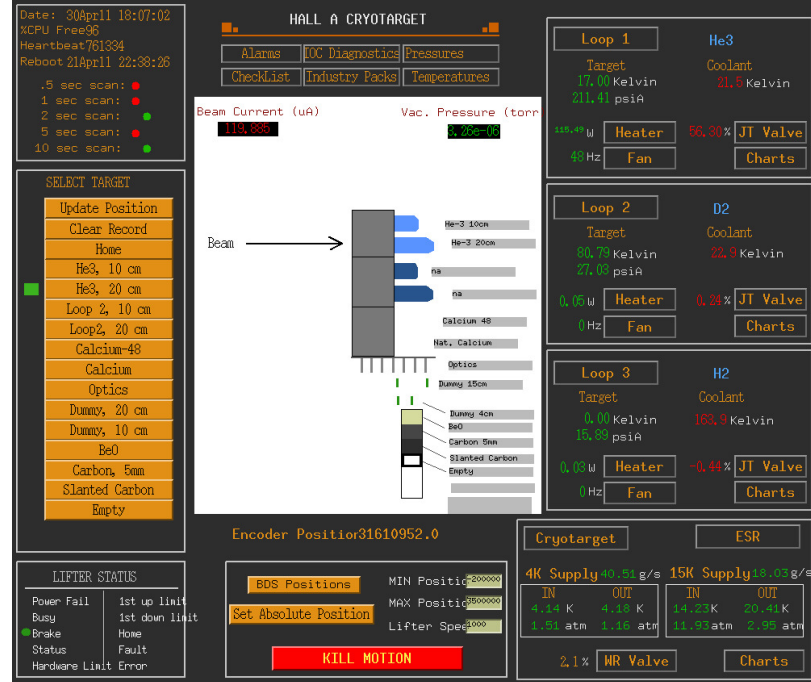
Figure 1.5: Picture of cryogenic target loops, where Loop-1 and Loop-2 include 10 cm and 20 cm aluminium cans, respectively. Loop-3 is not showed in this picture.

The target system is located in a scattering vacuum chamber, which is supported by a 607 mm diameter central pivot connected to two HRSs. The main part within the scattering chamber is a cryogenic target system, which includes three loops of cryogenic targets, a target ladder to support solid targets, sub-systems for cooling and gas handling, temperature and pressure monitors, and target control and motion systems [1]. Three target loops are named as Loop-1, Loop-2 and Loop-3, respectively. Loop-1 and Loop-2 both contain two aluminium target cells with lengths of 10 cm

and 20 cm, while Loop-3 has only a 20 cm cell (Fig. 1.5).



(a) First run period



(b) Second run period

Figure 1.6: Target control screen. Fig. 1.6a is the targeted installed in the first run period from before April 19th 2011, while Fig. 1.6b is the targets installed in the second run period after April 20th 2011.

The cryogenic targets used in this experiment were LD_2 , 3He and 4He . In the first run period of the experiment (from April 15th 2011 to April 19th 2011), the 20 cm cells of Loop-1 and Loop-2 were filled with 4He and LD_2 , respectively, as shown in Fig. 1.6a. 4He was then replaced by 3He in the second run period (From April 21st 2011 to May 15th 2011), and LD_2 was evacuated from Loop-2 (Fig. 1.6b). The 10 cm cell in Loop3 was used to store a ^{48}Ca foil which could not be directly exposed to the air. The temperature of LD_2 , 3He and 4He were maintained at 22 K , 20 K and 20 K , respectively. The cooling power was supported by the ESR [6] from JLab cryogenic group.

Target	ρ (g/cm^3)	Length (cm)	$\delta\rho$ (g/cm^2)	I (μA)	Comment
LD_2	0.1676	20.0		40	Loop2
Al can (Loop-2)	2.7	0.0272			Entrance
	2.7	0.0361			Exit
	2.7	0.0328			Wall
3He	0.0296	20.0		120	Loop1
4He	0.0324	20.0		90	Loop1
Al-can (Loop-1)	2.7	0.0272			Entrance
	2.7	0.0361			Exit
	2.7	0.0328			Wall
^{12}C	2.265	0.3937		120	
^{40}C	1.55	0.5735		40	
^{48}C	1.55	0.5284		40	
Dummy-20cm	2.7	0.1581			Upstream
	2.7	0.1589			Downstream
Dummy-10cm	2.7	0.1019			Upstream
	2.7	0.1000			Downstream

Table 1.1: Targets in E08-014 experiment, where BeO target and optics target are not listed.

Right after Loop-3 a 30 cm long optics target was installed for taking optics calibration data. The optics target contains 7 carbon foils located at -15 cm , -10 cm , -5 cm , 0 cm , 5 cm , 10 cm , and 15 cm , respectively. Two dummy targets, *Dummy-20cm* and *Dummy-10cm*, were installed to measure contributions from the end-cups of cryogenic target cells. Each target contains two thick aluminium foils separated by

10 cm for *Dummy-10cm* and 20 cm for *Dummy-20cm*. There were four other targets, BeO, ^{12}C , ^{40}Ca and an empty target, installed on the target ladder.

The list of targets used in this experiments is given in Table 1.1 and a report that contains detailed information of targets and related systems can be found in [7]. The actual target positions are required to be surveyed during the experiment. However, survey reports were only available for experiments ran before this experiment. The targets were reinstalled in the second run period but the extract position remained unknown. The relative positions with respect to the central foil of the optics target can be evaluated during the pointing study.

1.4 High Resolution Spectrometers

The essential equipments in Hall-A are two identical HRSs which provide high momentum resolution at the 10^{-4} level over the range from 0.8 to 4.0 GeV/c , high position and angular resolution in the scattering plane, and large angular acceptance. As shown in Fig. 1.4, the spectrometer on the left of the beam direction (to the beam dump) is called HRS-L, and the other one on the right is called HRS-R. The basic layout of a HRS is given in Fig. 1.7, where the magnet configuration of each HRS is QQDQ, including three superconducting $\cos(2\theta)$ quadrupole and an indexed dipole. Two quadrupole, Q1 and Q2, are installed in front of the dipole to achieve the desired angular acceptance and maximize the resolving power for the bend angle. The dipole performs 45° vertical bending of charged particles, and additionally, accommodates the extended targets and focuses the parallel beam. The third quadrupole, Q3, is behind the dipole to enhance the position and angular resolutions. Some important characteristics of HRSs are listed in Table 1.2.

The power supply for Q3 on HRS-R (RQ3) was defected during the experiment and limited the maximum central momentum setting to 2.876 GeV/c , although the

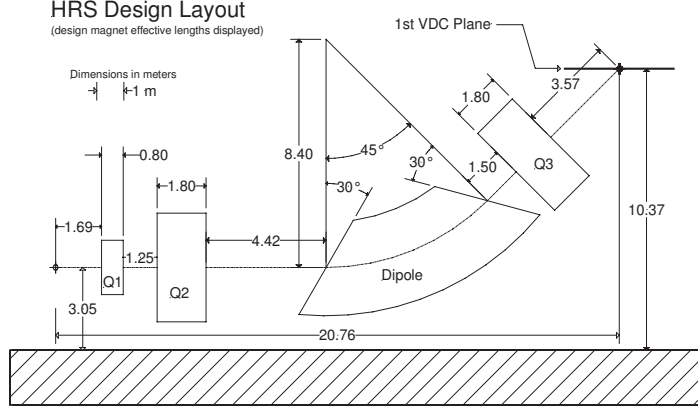


Figure 1.7: Schematic layout of Schematic layout of HRS,which shows the sizes and locations of the dipole and three quadrupole [1].

Bend Angle:	45°
Optical Length:	23.4 m
Momentum Range:	0.3-4.0 GeV/c
Momentum Acceptance:	$-4.5\% < \delta p/p < +4.5\%$
Momentum Resolution:	1×10^{-4}
Angular Range	$12.5 - 150^\circ$ (HRS-L), $12.5 - 130^\circ$ (HRS-R)
Angular Acceptance:	± 30 mrad (Horizontal), ± 60 mrad (Vertical)
Angular Resolution:	0.5 mrad (Horizontal), 1.0 mrad (Vertical)
Solid Angle:	6 msr at $\delta p/p = 0, y_0 = 0$
Transverse Length Acceptance:	± 5 cm
Transverse Position Resolution:	1 mm

Table 1.2: Design characteristics of HRSs, where the resolution values are for the FWHM [1].

experiment run plan required the maximum central momentum to be 3.055 GeV/c on this spectrometer. The RQ3 field was scaled down to 87.72% of its normal value for each setting, which allowed only one set of optics matrix for all data. However, the standard HRS-R optics matrix was not able to apply on the data. An optics calibration procedure to obtain the new optics matrix and any corrections will be discussed in next chapter.

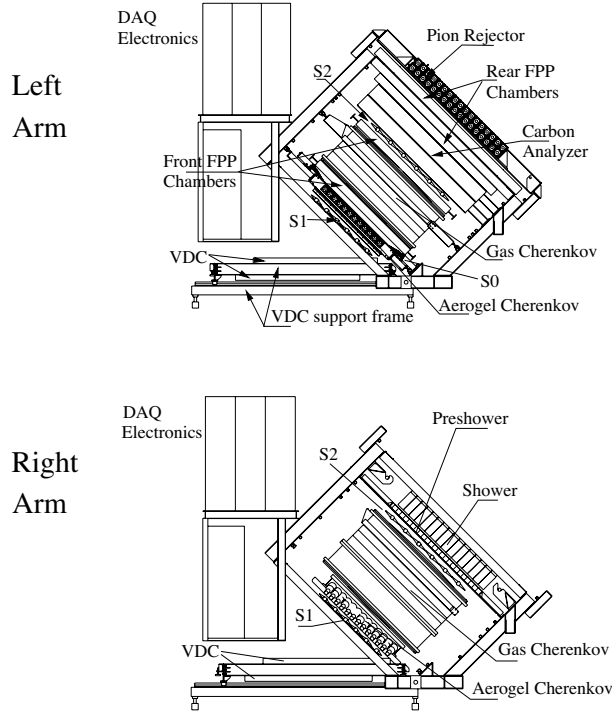


Figure 1.8: Detector Stack

1.5 Detector Packages

As shown in Fig. 1.8, the detector package in each arm includes two vertical drift chambers (VDCs), two scintillator planes (S1 and S2m), a gas Cherenkov detector (GC), and a calorimeter. In addition to these standard detectors, a long single-bar scintillator (S0) and an Aerogel Cherenkov detector (AC) are equipped in each HRS, and a focal plane polarimeter (FPP) is only available in HRS-L. S0, AC and FPP were not used during this experiment.

Particles coming through the HRS are fully characterized by the detector package and their signal outputs are delivered to the front-end electronics to form trigger signals and to be recorded by the data acquisition (DAQ) system. Signals from VDCs

are converted into digital types by the discriminator cards attached on the VDCs and then sent directly into the front-end of the time-to-digital converter (TDC) on the FastBus crate.

For all other detectors, each analog signal from the corresponding photomultiplier tube (PMT) is split into two copies, one of which is properly delayed though a long cable before it is fed into the front-end of analog-to-digital converter (ADC), and at the same time, the other one of which goes through the discriminator module (DIS) and if its amplitude is over the threshold value, a digital signal will be created and further used to form trigger signals or be recorded by the TDC front-end.

The design and performance of each detector will be discussed in the following.

1.5.1 Vertical Drift Chambers

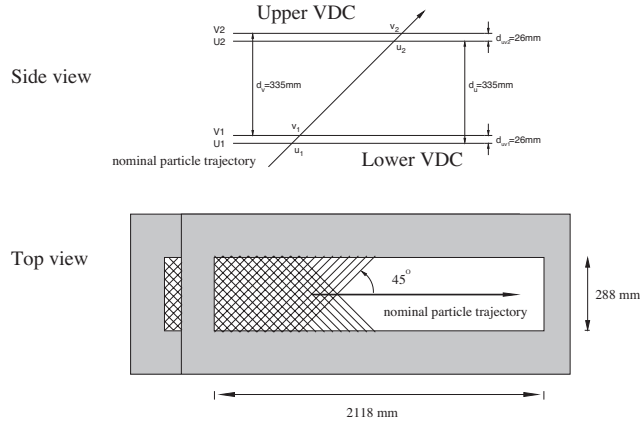


Figure 1.9: Layout of VDCs

The trajectory of particles after the Q3 exit is tracked by two identical VDCs, which are placed vertically 335 mm apart and inclined by 45^0 along the normal particle trajectory [1], as shown in Fig. 1.9. There are two wire planes (U and V) in each VDC and each plane contains 368 wires, which are oriented at 90^0 for one

another. Two gold-plated Mylar planes are placed below and above each wire plane, and an high electric field is generated by applying -4 kV between the wire plane and each Mylar plane. Both VDCs are filled with argon (68%) and ethane (38%) with a flow rate of 10 liter/hr .

When a particle goes through the VDC, the gas molecules can be ionized and create a bunch of electrons and ions on the trajectory of the particle. The electrons are accelerated by the high field toward the closest wires, and the signal collected by each wire is amplified and read out by a pre-amplifier TDC card. On average, five sense wires have read-out signals when a particle passes through each wire plane. The exact location where the particle hits on the plane can be reconstructed by those TDC signals. Four wire planes provide four locations which are used to fit the trajectory of the particle. The position resolution in the focal plane is $\sim 100\mu\text{m}$ and the angle resolution is $\sim 100\text{ mrad}$.

1.5.2 Scintillator Counters

Two scintillator planes, S1 and S2m, are placed after VDCs and separated by 2 m apart. S1 is composed of six overlapping thin plastic paddles, and S2m has 16 smaller paddles. When a charge particle passes through the paddle, it creates light which travels toward both ends of the paddle. A PMT on each end of the paddle collects the light and converts it into a analog signal. Scintillators have very fast time-response with very good resolution ($\sim 30\text{ ns}$), so their signals are mainly used to generates triggers for the DAQ system. The traditional production trigger in Hall-A is generated by requiring both S1 and S2m to be fired within a narrow time windows. A detailed discussion of trigger system is given in Section 3.7 and Appendix A.

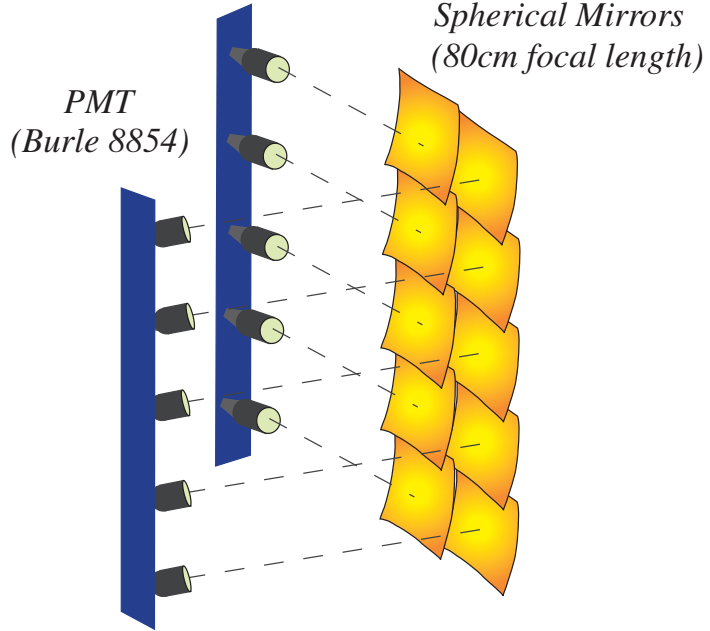


Figure 1.10: Design of Cerenkov Detector

1.5.3 Gas Cherenkov Detectors

A high energy charged particle radiates Cherenkov light when it travels in a medium with its velocity faster than the speed of light. The basic mechanism of Cherenkov radiation is that atoms along the track of the particle are polarized and become dipoles, and the variation of dipole moments emits electromagnetic light [8]. The angle between the direction of Cherenkov light and the track of the charge particle is given by:

$$\cos\theta = \frac{1}{\beta n}, \quad (1.2)$$

where n is the index of reflection of the medium, and $\beta = v/c$.

The velocity-dependence property of Cherenkov radiation provides an effective tool to discriminate particles with different masses, utilizing the mass-dependence of the momentum threshold to emit Cherenkov light:

$$P_{threshold} = \frac{mc}{\sqrt{n^2 - 1}} \quad (1.3)$$

A gas Cherenkov detector (GC), made up of a steel box with thin entry and exit window, is mounted between S1 and S2m on each HRS. Within the box ten light-weight spherical mirrors with very small thickness (0.23 gcm^2) are positioned in a 2 (horizontl) \times 5 (vertical) array, as shown in Fig. 1.10hy. These mirrors are carefully arranged to efficiently reflect and focus the Cherenkov light on the associated ten PMTs.

The GC box is filled with atmospheric pressure CO_2 , which gives the index of refraction to be 1.00041. The momentum threshold for electrons to radiate Cherenkov light in this detector is about 18 MeV/c, while the threshold for pions is as high as 4.9 GeV/c. Since the momentum coverage of HRS is from 0.5 GeV/c to 4.0 GeV/c, only electrons can emit Cherenkov light in the detectors. Pions may still be able to produce signals in the GC when they interact the gas and create low-energy electrons ($\delta - electrons$). However, the probability of such process is relatively low and the amplitude of the signal is comparable to the background signal. The path length of the GC on HRS-L is 80 cm which yields an average of 7 photon-electrons, while on HRS-R, the path length for the GC is 130 cm , leading to 12 photon-electron on average [1]. The design of GCs provides excellent electron identification (99%).

The signal from each PMT is amplified by 10 times by an amplifier then divided into two copies. One copy is directly sent to the front-end ADC for offline analysis. The other copy is further split into two pieces, one of which is converted into a digital signal and sent to the TDC, while the other of which is added together with similar signals from other 9 PMTs. The sum of the ten signals is then converted into a digital signal which is used for the design of online triggers, such as the efficiency triggers. During E08-014, GCs were also included in the production triggers to suppress pion events during the data recording.

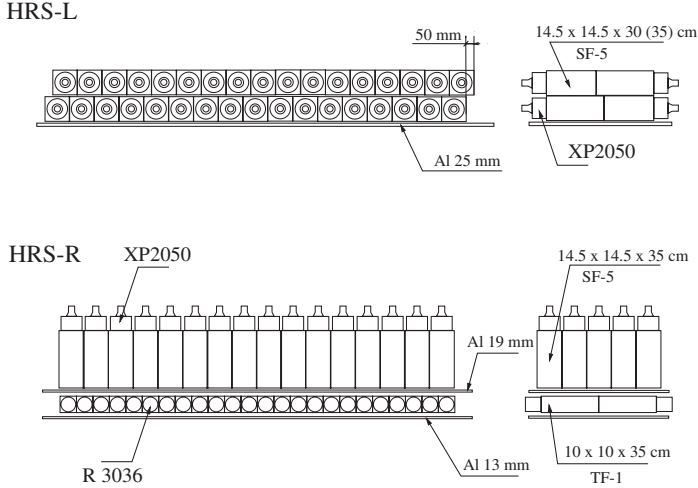


Figure 1.11: Schematic layout of Pion Rejectors in HRS-L and Shower counters in HRS-R.

1.5.4 Lead Glass Calorimeters

In each HRS, a calorimeter is placed behind S2m for the energy measurement of charge particles. Each calorimeter is composed of two layers of lead glass blocks and associated PMTs (Fig. 1.11). The gaps between blocks in the first layer is covered by the blocks in the second layer. The two layers of the calorimeter in HRS-L are called Pion-Rejector-1 (PRL1) and Pion-Rejector-2 (PRL2), respectively), and each layer consists of two columns of 17 lead glass blocks. In HRS-R, the first layer of the calorimeter, also named as PreShower (PS), is formed by two column of 24 lead glass blocks, while the second layer, called Shower (SH), includes two columns of 16 lead glass blocks. Two PMTs are attached to each block to collect the photon signals.

When propagating through the dense material, a high energy charged particle loses its energy exclusively due to Bremsstrahlung effect. The emitted photons sequentially create electron-positron pairs which generate secondary Bremsstrahlung radiation. For a long enough path length in the material, an electromagnetic cascade is developed along the direction of incident particle. At the GeV energy scale, only electrons are able to develop such a cascade in the HRS calorimeter. Since heavier particles require

a much longer path length, the calorimeter provides a useful substantial particle identification in addition to the GC. PS and SH together form a total absorber since they use much thicker lead glass blocks which can absorb the entire electromagnetic shower produced by the incident electrons. PRL1 and PRL2 still provide powerful capability of electron identification even though they don't form a total absorber.

1.6 Data Acquisition System

The data-acquisition (DAQ) system in Hall-A is composed of the CEBAF online data acquisition system (CODA) developed by the JLab CODA group, and the associated hardware components. CODA is a tool-kit of software components, including read-out controllers (ROCs), the event builder (EB), the event recorder (ER) and the event-transfer (ET), as well as the RunControl (RC). The RC is a graphical user interface to select experimental configurations, to start and stop runs, and to monitor and reset CODA components [1]. The hardware elements are basically composed of front-end Fastbus, VME devices (ADCs, TDCs and scalers), VME-Fastbus interface, single-board VME computers, trigger supervisors (TS) and network components. CODA is operated on a Linux based workstation which stores the recorded data (called raw data) in the local hard-drive. The data is subsequently transferred to a mass storage tape silo (MSS) for long term storage. Data in the local hard-drive will be deleted when the size reaches a certain percentage of the entire hard-drive space.

E08-014 experiment ran consecutively with four other experiments during the spring of 2011. Besides HRSs, there were two other spectrometers, BigBite and Neutron-Detector, which were installed in the hall for double-coincidence and triple-coincidence experiments. Triggers from four spectrometers were sent to the same TS located in the electronic hut on the floor. When a trigger was accepted by the TS, a Level-One-Accept (L1A) signal was generated and sent back to each spectrometer.

The leading-edge of the L1A signal was then adjusted by the strobe signal in a retiming-module (RT) installed in the local front-end crate. The signal from RT was fed to the Transition Module (TM) [9], where an ADC gate, a TDC Start/Stop signal and control signals were generated and distributed to the front-end electronics on Fastbus crates and VME crates, such as ADCs, TDCs and scalers. An event number associated with this trigger was registered in the DAQ system and all signals associated with this events were recorded.

Limited by the dead-time and data size, not all triggers were accepted by the TS. A pre-scale factor was assigned to each trigger type to control the total event rate before CODA starts taking data. For example, a pre-scale factor "3" represents only the first one is accepted for every three consecutive events from the trigger, while a pre-scale factor "0" means that any events from the trigger will not be recorded. Each time when CODA starts to take data, an unique run number is given to the raw data file which stores all events coming after the start of the run. To control the total size of the data file and to prevent the data file from being damaged by any errors during the data taking, CODA will be stopped when each run reaches a pre-defined length of time or a certain number of events, and then a new run will be started with a new run number.

Scaler events are read for every 1-4 seconds to provide the online dead-time estimation and other calculations, for example, to extract total accumulated electron charge. Meanwhile, EPICS (the Experimental Physics and Industrial Control System) data from the slow control systems, such as beam energy, readings from BPMs and BCMs, target temperature and pressure monitors, spectrometer angles and magnet fields and etc., are also inserted into the data stream for every few seconds.

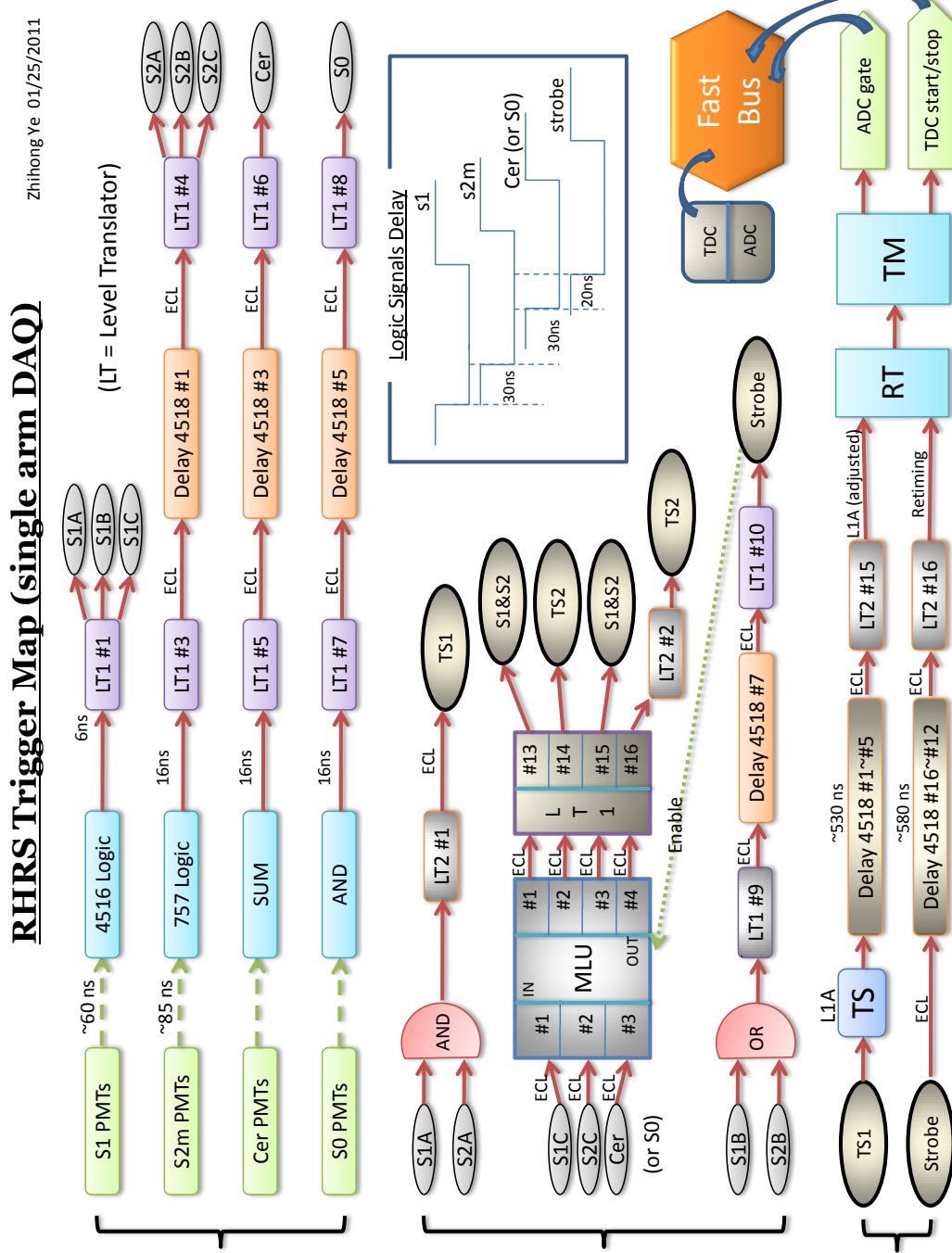


Figure 1.12: Single arm trigger design on HRS-R. The HRS-L trigger has the similar layout except some electronic modules were different.

1.7 Trigger Design

Only two HRSs were used to take data during E08-014. Other spectrometers were turned off and their triggers were all ignored. The design of the trigger system in both HRSs were identical, and the detailed sign of HRS-R triggers is illustrated in Fig. 1.12. Three detector planes, S1, S2m and GC were involved in the trigger design. For S1 or S2m, a logic signal was created when one or more scintillator bar in the plane was fired. The logic signal of the GC was the digital signal converted from the sum of ten PMT signals. The *AND* of logic signals from S1, S2m and GC creates T1 (T3) trigger in HRS-R (HRS-L), which is the production trigger in this experiment. T3 (T4) was formed in HRS-R (HRS-L) by the coincident signal of the GC logic signal and only one of the S1 or S2m logic signal. T3 (T4) was designed to evaluate the trigger efficiency of T1 (T3). For some other experiments, T3 and T4 were designed by replacing the GC with S0. T6 (T7) is generated from the overlapped signal of S1 and S2m which is the traditional HRS main trigger. Events from T6 and T7 were used for particle identification study since pions were also recorded. T5 is the coincident signal of T1 and T3, and was disabled in this experiment. A discussion of triggers during the data analysis is given in Apendex A.

Chapter 2

Calibration

Experimental data collected by the DAQ system is stored in raw data files, each of which is assigned with an unique run number. A raw data file, generally called a run, contains plentiful information, including the experimental settings during the run and all the signal readouts from experimental instruments for each event. However, those information can not be directly read out from the raw data file. The Hall A C++ Analyzer [10], an object-oriented framework on top of ROOT [11] and developed by the Hall A software group, is used to replay the raw data and calculate importance quantities which are stored in ROOT files, which can then be directly accessed through the ROOT interface or C/C++ subroutines. Each ROOT file contains several subdirectories which are called "trees". The event-by-event detector readouts, including both the uncalibrated and calibrated signals are stored in the **T** tree. The EPICS readings are put in the **E** tree, and the **RIGHT** tree and **LEFT** tree store signal readouts from scalers in HRS-R and HRS-L, respectively. To extract the correct information, the name of the signal readout and its corresponding electronic map, such as the front-end crate number, the electronic module's type and slot ID in the crate, and the channel number which the signal cable connects to, have to be specified and updated in the data base (DB) of the Analyzer.

The data base of each instrument also contains the calibration constants which converted the raw signals into meaningful quantities which can be used for further data analysis. The first step of the data analysis is to obtain those calibration constants for each instrument using calibration data, which will be discussed in this chapter. After the data bases are updated, the raw data will be replayed again and the new ROOT files can be used to extract useful physics quantities, for example, extracting cross sections, given in next chapter.

2.1 Calibration Overview

The calibration is composed of three major parts: beam instruments, detector packages and optic matrices of HRSs.

The calibration of beam instruments aims to obtain the constants of the beam position monitors (BPMs) and the raster system to locate the event-by event beam position, and calibrate the beam charge monitors (BCMs) to calculate the accumulated beam charge. The beam position calibration has been proceeded during the experiment by using the Harp scan data [12]. The detailed calibration procedure of the BPMs and the raster system can be found in the reference [2]. The result of BCM calibration is given in this report [3], and the calculation of beam charge will be presented in Section 5.2.

Each detector in the HRS can be individually calibrated, while the calibration of HRS optics requires a good determination of the beam position and an updated reference time (T_0) for each VDC wire. T_0 can be changed when the data bases of S1 and S2m are updated. In this experiment, S1 and S2m was unable to be calibrated because of several bad TDC channels, and the values of T_0 were updated in the VDC data base using old S1 and S2m data bases. The detailed calibration of the gas Cherenkov detectors, calorimeters and the HRS optics will be given in next two

sections.

2.2 Detector Calibration

The signal produced by the incident particle is collected by PMTs attached on the detector. The GC in each HRS contains 10 PMTs. Each layer of the calorimeter in HRS-L (PRL1 and PRL2) has 34 PMTs, and the calorimeter in HRS-R has 48 and 32 PMTs in PS and SH, respectively.

For each trigger event, the signal output from each PMT is split into the digital format and the analog format, which are then recorded in the TDC and the ADC front-ends, respectively. For the common-stop TDC module, the channel number in the TDC spectrum represents the time difference between when the event triggers and when the STOP signal arrives. The channel number in the ADC spectrum, on the other hand, is directly related to the strength of the PMT signal. However, the PMT signal not only is proportional to the photon energy, but also depends on the high voltage applied on the PMT as well as the amplitude of the background signal. One needs to obtain the gains factor which converts the channel number into a common energy scale for all PMTs in the same detector. After updating the gain factors in the data base, the calibrated ADC spectra can be added up together to obtain the total photon energy released in the detector by the particle.

2.2.1 Gas Cherenkov Detectors

A calibration procedure of the GC aims to align the single photon electron (SPE) peak in each ADC spectrum to 100 channels. The gain factor for the *i*th PMT are defined as:

$$C_i = \frac{100}{M_i^{SPE} - M_i^{pedestal}} \quad (2.1)$$

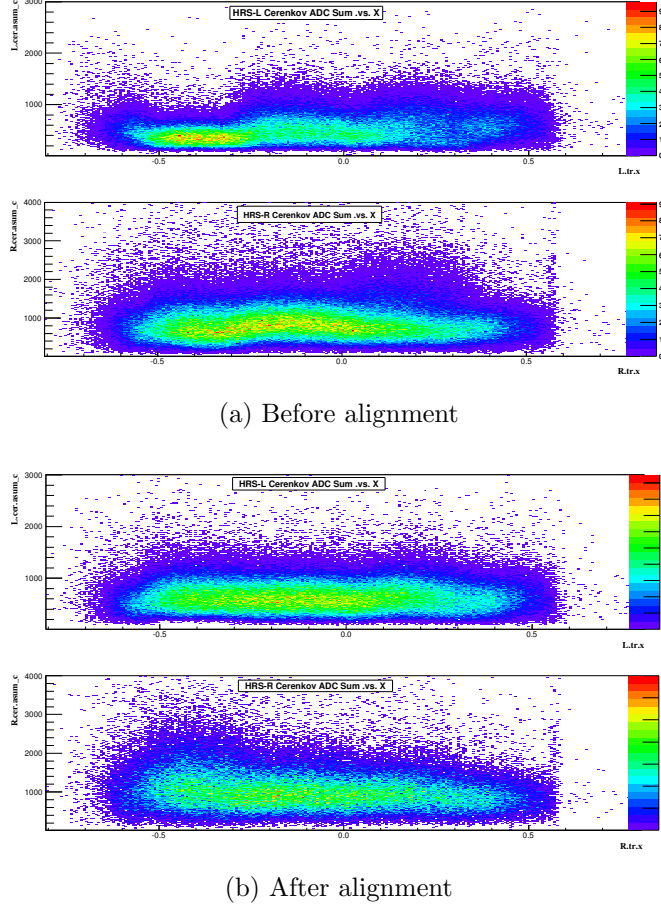


Figure 2.1: Alignment of gas Cherenkov detectors. The 2-D histogram in each plot is the sum of the GC ADC spectra vs x_{fp} , which give the arrangement of ten GC PMTs. Plots in (a) show that the ADC peaks are off by certain channels before the calibration, while plots in (b) demonstrate that those peaks are nearly at the same channel number after the alignment.

where M_i^{SPE} and $M_i^{pedestal}$ are the mean values of the SPE peak and the pedestal peak in the i th ADC spectrum.

The calibration was performed using events from T6 and T7, since the SPE peaks are not significant in the main production triggers ($T1\&T3$) which includes the GC. Fig. 2.1 shows that the ADC spectra were well aligned for the GC in each arm. The sum of ten calibrated ADC spectra, $L.cer_asum_c$ for HRS-L or $R.cer_asum_c$ for HRS-R, clearly shows the SPE peak located at 100 channel (Fig. 2.2), and can be directly applied on the particle identification.

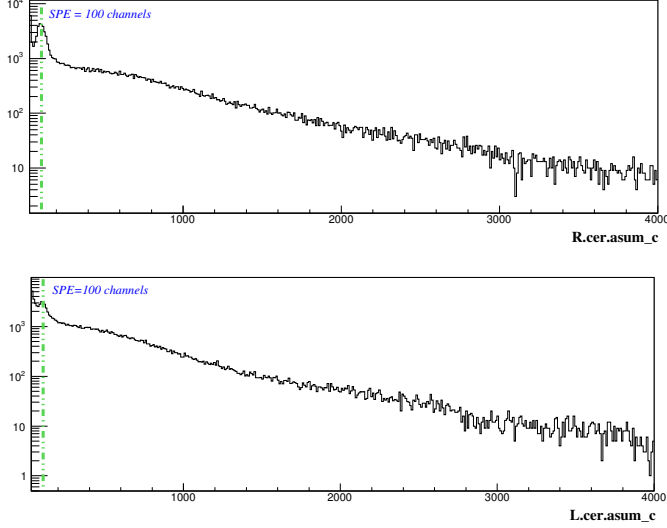


Figure 2.2: Single photon electron peaks in the sum of the GC ADC spectra. Top for HRS-L and Bottom for HRS-R.

2.2.2 Electromagnetic Calorimeters

The design of Hall-A calorimeters enables the few GeV electrons to deposit their energies entirely in term of light in the detectors. The electron creates a track during the cascade, and lead glass blocks along the track collect the most strong photon signals. During the data replay, these blocks can be identified by using the VDC tracking information, and the group of these blocks is called a cluster. The sum of their ADC spectra after the calibration, e.g., $L.prl1.e$ for PRL1, denotes the energy deposited in this cluster, and should be distinguished from the sum of the calibrated ADC spectra of all blocks in the layer, e.g., $L.prl1.asum_c$, although they are equal when all energy are completely deposited in the cluster and the background signals are small.

Once the individual ADC spectrum is calibrated, the sum of the energy deposited in the two clusters, e.g., $L.prl1.e+L.prl2.e$, should be equal to the energy of scattered electrons. A new variable, E/P , is defined as the ratio between the sum and the electron's momentum, e.g., $E/P = (L.prl1.e + L.prl2.e) / (P_0 \cdot (1 + L.tr.tg_dp))$,

and should be centered at one if the gain factors are properly calibrated. Different procedures were applied on each calorimeter.

The performance of energy measurement is limited by the design of calorimeters, as well as the energy range and the type of charge particles. In general, the energy resolution of a calorimeter can be represented by [8]:

$$\frac{\sigma(E)}{E} = a \oplus \frac{b}{\sqrt{E}}, \quad (2.2)$$

where \oplus represents two terms added in quadrature. The first term is mainly contributed by systematic errors, such as intrinsic shower fluctuations, which should be small for homogeneous calorimeters, such as total absorbers. The value of second term is determined by the uniformity of calorimeters as well as uncertainty of detector calibration. It is typically $5\%/\sqrt{E}$ for lead glass calorimeters.

A minimization method was used to calibrate Pre-Shower (PS) and Shower (SH) [13], and the Chi-Square is defined as:

$$\chi^2 = \sum_{i=1}^N \left[\sum_{j \in M_{ps}^i} C_j \cdot (ADC_j^i - Ped_j) + \sum_{k \in M_{sh}^i} C_k \cdot (ADC_k^i - Ped_k) - P_{kin}^i \right]^2 \quad (2.3)$$

where i is the i th event; j is the j th PS block; k is the k th SH block; M_{ps}^i and M_{sh}^i are sets of PS and SH blocks included in the reconstructed cluster for the i th event; $ADC_{j/k}^i$ and $Ped_{j/k}$ represent the ADC channel number of the event and mean pedestal value in the ADC spectrum, respectively; P_{kin}^i is the particle momentum of the i th event; and $C_{j/k}$ is the gain factor of the ADC spectrum used as a fitting parameter during the minimization.

To obtain the best fitting result, electron samples were selected from data taken at the kinematics region of QE tail, where scattered electrons uniformly distribute among all lead glass blocks. A Fumili minimization package [14] was called to minimize χ^2 ,

and the gain factors obtained from the fitting parameters were stored in the database.

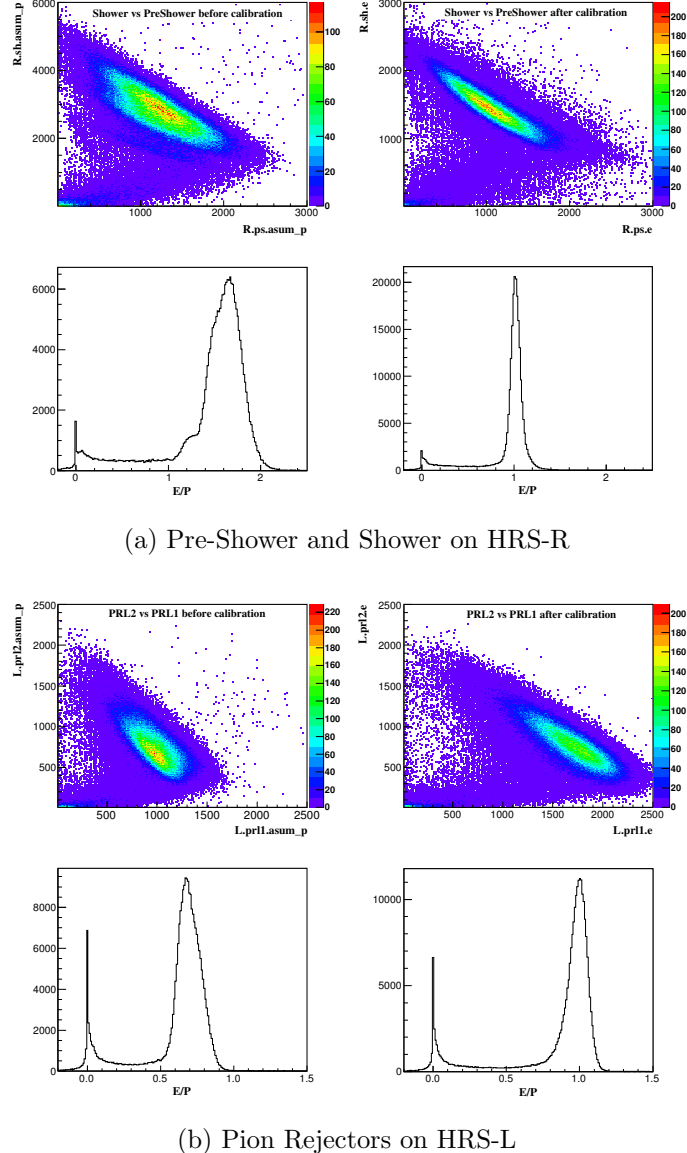


Figure 2.3: Calibration of calorimeters. In each figure, the top two plots are the 2-D histograms of the PS (PRL1) ADC sum versus the SH (PRL2) ADC sum before and after the calibration. The electron band is clearly isolated after the calibration. The bottom two 1-D histograms are the distributions of E/P before and after the calibration. The peak becomes sharp and locates at one with new gain factors.

Similar to the idea of the GC calibration, the calorimeter on HRS-L was calibrated by aligning the minimum ionization peak of each ADC spectrum to a common channel

number. The cosmic ray events were used during the calibration since they were uniformly distributed along the entire blocks. Furthermore, the particles in cosmic ray are mostly muons, which have small energy spread. The pedestal peak (ADC_i^{ped}) and muon peak (ADC_i^{muon}) in the ADC spectrum of the i th PMT were located and their distance were aligned to 100, by applying a gain factor defined as:

$$C_i = \frac{100}{ADC_i^{muon} - ADC_i^{ped}} \quad (2.4)$$

The E/P was calculated by using the calibration data replayed after updating the data base with new gain factors for all PMTs. The gain factors were further adjusted with a common value to shift the peak to one:

$$C_i^{real} = C_i \times \frac{1}{M_{E/P}} \quad (2.5)$$

where $M_{E/P}$ represents the mean value of the E/P peak before the adjustment. The adjusted gain factors were then updated in the data base.

The results of the calibration are shown in Fig. 2.3a and Fig 2.3b, where electrons are better separated from backgrounds and E/P is well centered at one. The locations of E/P peaks at different momentum settings were shown in Fig. 2.4, where the energy resolutions of calorimeters were also given by fitting the spread of E/P peaks as functions of the momentum values. The total resolution of PS and SH is 2.53% per GeV. The resolution of Pion Rejectors is 3.21% per GeV which is slightly worse because they are not total absorbers.

2.3 HRS Calibration

After coming out from the target chamber, a charged particle travels a long distance within the HRS, and its trajectory after the Q3 exit is tracked by two VDCs which

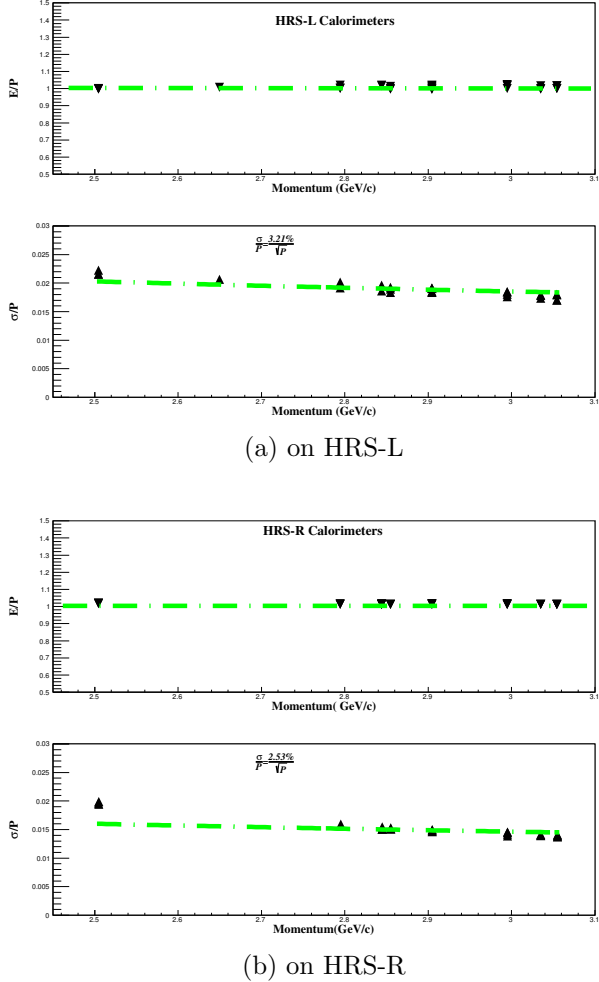


Figure 2.4: Calibration performance and resolution of calorimeters. The top plot in each figure reveals the performance of calibration at different momentum setting. The two bottom plots give the resolution of calorimeters, which are 3.21% on HRS-L and 2.53% on HRS-L.

specify its position and direction at the focal plane. By using the focal plane quantities, an optics matrix reconstructs the particle's position and direction at the target plane where the electron interacts with the target.

The standard HRS optics matrices have already been extracted in previous Hall-A experiments. However, the absolute positions of the target, the HRS and detectors change from time to time, and these offsets should be taken into account in the optics matrices. Furthermore, during E08-014 experiment, the magnet field of the third Quadrupole in HRS-R (RQ3) was limited to 2.8273 GeV/c due to a power supply

issue, while our maximum momentum setting was 3.055 GeV/c. The RQ3 field had to be scaled down to 87.72% of the dipole field for each setting, so the old HRS-R optics matrix was not applicable. In this section, a calibration procedure to obtain new optics matrices for this experiment will be introduced.

2.3.1 Coordinator Systems

Coordinates used during data analysis are briefly presented here. A more detailed description of Hall A coordinate systems and the transportation between coordinates is given in reference [15]. Notes that angles defined in all coordinates are actually the tangent of their values.

- **Hall Coordinate System (HCS)**

The center of the HCS is defined as the intersection of the beam and the vertical axis of the target system. \hat{z} is along the direction of the beam, \hat{x} is to the left of \hat{z} and \hat{y} is vertically up (Fig.2.5).

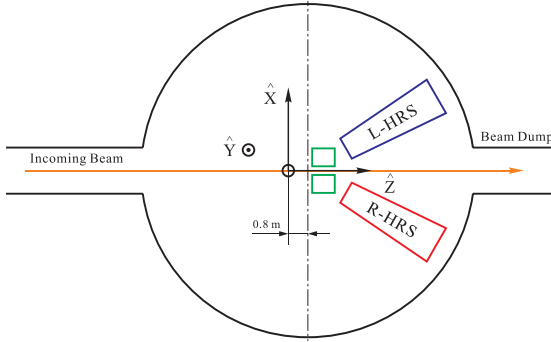


Figure 2.5: Hall Coordinate System (HCS)

- **Target Coordinate System (TCS)**

As shown in Fig.2.6, \hat{z}_{tg} is the direction from the target system perpendicularly going through the center hole of the sieve slit plane on each spectrometer. The

origin of TCS is given by the intersection of \hat{z}_{tg} and the vertical axis of the target system, and L is a constant length from the origin of TCS to the sieve slit plane. \hat{x}_{tg} is parallel to the sieve slit plane and vertically down, and \hat{y}_{tg} is to the left of \hat{z}_{tg} . $\hat{\theta}_{tg}$ (the out-of-plane angle) and $\hat{\phi}_{tg}$ (the in-plane angle) are taken to be dx_{sieve}/L and dy_{sieve}/L . The origins of HCS and TCS are not necessarily overlapped and the value of D , the offset between two position, changes when moving HRSs to different angles. Surveys is required during the experiment running to obtain the offset value.

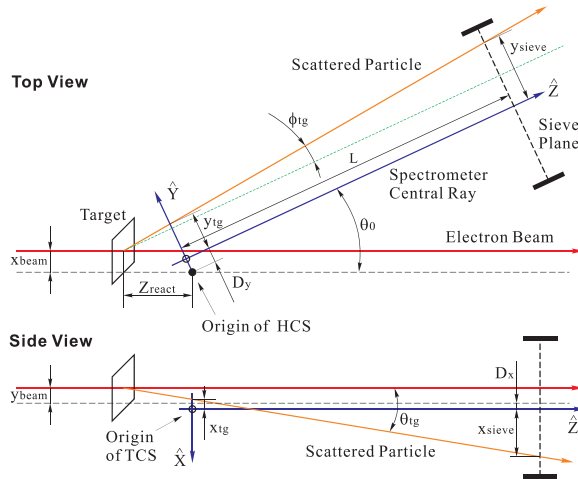


Figure 2.6: Target Coordinate System (TCS)

- **Detector Coordinate System (DCS)**

The origin of DCS can be defined as the intersection point of the wire 184 of U1 plane and the wire 184 of V1 plane on the first VDC (VDC1). \hat{z}_{det} is perpendicular to the VDC planes away from HRS, \hat{x}_{det} is horizontally along the long symmetry axis of lower VDC pointing away from the hall center, and \hat{y}_{det} is vertically up toward \hat{z}_{det} (Fig. 2.7).

- **Transport Coordinate System (TRCS)**

The TRCS is generated by rotating the DCS clockwise around \hat{y}_{det} by 45^0 (Fig. 2.8).

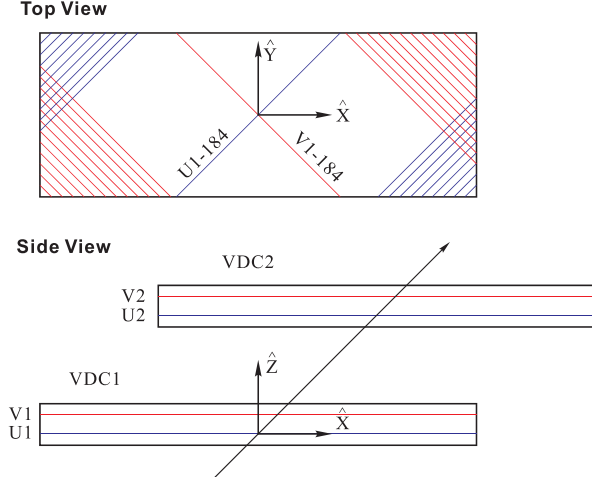


Figure 2.7: Detector Coordinate System (DCS)

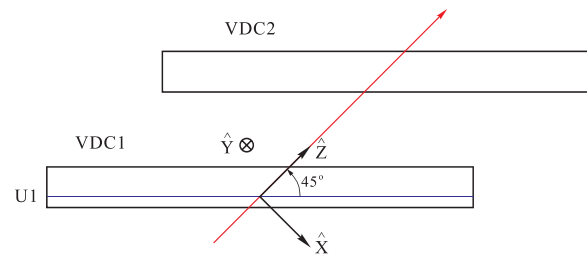


Figure 2.8: Transport Coordinate System (TRCS)

- **Focal Plane Coordinate System (FCS)**

The FCS is obtained by rotating DCS around its \hat{y}_{det} axis by an angle ρ , which is the angle between \hat{z}_{det} axis and the local central ray with $\hat{\theta}_{tg}=\hat{\phi}_{tg}=0$ for the corresponding relative momentum $\delta p = (p - p_0)/p_0$ (Fig.2.9).

2.3.2 Optics Optimization

The optics calibration basically follows the procedure described in the reference [15]. A optics matrix for HRS is a set of polynomial transportation functions to calculate the target plane quantities, δp , y_{tg} , θ_{tg} and ϕ_{tg} , by using the focal plane quantities,

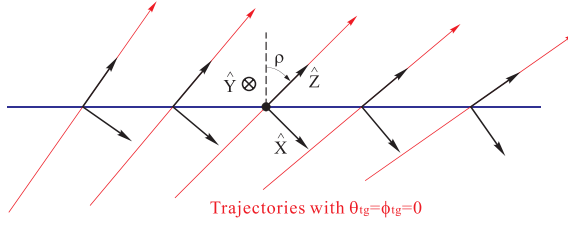


Figure 2.9: Focal Plane Coordinate System (FCS)

x_{fp} , y_{fp} , θ_{fp} and ϕ_{fp} . The functions are given by:

$$\delta p = \sum_{i,j,k,l} C_{ijkl}^D x_{fp}^i \theta_{fp}^j y_{fp}^k \phi_{fp}^l, \quad (2.6)$$

$$y_{tg} = \sum_{i,j,k,l} C_{ijkl}^Y x_{fp}^i \theta_{fp}^j y_{fp}^k \phi_{fp}^l, \quad (2.7)$$

$$\theta_{tg} = \sum_{i,j,k,l} C_{ijkl}^T x_{fp}^i \theta_{fp}^j y_{fp}^k \phi_{fp}^l, \quad (2.8)$$

$$\phi_{tg} = \sum_{i,j,k,l} C_{ijkl}^P x_{fp}^i \theta_{fp}^j y_{fp}^k \phi_{fp}^l, \quad (2.9)$$

where D terms (C_{ijkl}^D), Y terms (C_{ijkl}^Y), T terms (C_{ijkl}^T), and P terms (C_{ijkl}^P) represent the matrix elements of δp , y_{tg} , θ_{tg} and ϕ_{tg} , respectively. An optics calibration procedure is set to determine the matrix elements by using the optics data taken during the experiment.

There are three new variables in HCS which are more practical for long targets and foil targets with known offsets from the hall center:

$$z_{react} = -(y_{tg} + D) \frac{\cos \phi_{tg}}{\sin(\Theta_0 + \phi_{tg})} + x_{beam} \cot(\Theta_0 + \phi_{tg}), \quad (2.10)$$

$$y_{sieve} = y_{tg} + L \cdot \tan \phi_{tg}, \quad (2.11)$$

$$x_{sieve} = x_{tg} + L \cdot \tan \theta_{tg}, \quad (2.12)$$

	Angle	D_x (mm)	D_y (mm)	D_z (mm)	Survey Report
HRS-L	21.480	1.78	1.25	-0.70	DVCS [16]
HRS-R	-20.022	-2.91	0.73	-1.06	PVDIS [17]

Table 2.1: Spectrometer offsets for survey reports, where D , the offset between the origins of HCS and TCS, is given in term of three components in HCS.

	L (mm)	x_{sieve} (mm)	y_{sieve} (mm)	Survey Report
HRS-L	1182.3	-1.05	0.20	DVCS [16]
HRS-R	1175.9	1.04	0.05	A1n [18]

Table 2.2: Sieve slit plates offsets from survey reports. The values were measured in HCS.

where x_{beam} is the horizontal position of the beam, θ_0 is the central angle of the spectrometer, and L and D are defined in TCS. z_{react} is the reaction location along the beam direction and also provides the target position in HCS. x_{sieve} and y_{sieve} represent the vertical and horizontal positions at the sieve slit plane. During the experiment, the beam position was locked at (-2.668 mm, 3.022 mm). Table 2.1 and Table 2.2 give the values of D , x_{sieve} and y_{sieve} from survey reports.

As given in table 2.3, a group of optics data has been taken during the experiment with the optic target which was used to calibrate y_{tg} . When taking angular calibration data, a sieve slit plate (Fig. 2.10) was attached on the entrance of Q1 for each HRS. The data was taken at QE region to ensure each hole on the sieve slit plate was covered with enough statistics.

Run Number	Target	Angle	P_0/P_0^{RQ3} (GeV/c)	Raster	Sieve	Comment
3695	Dummy4cm	23^0	2.678/2.3492	Off	Out	$\delta p +3\%$
3698	Dummy4cm	23^0	2.600/2.2808	Off	Out	$\delta p 0\%$
3704	Dummy4cm	23^0	2.522/2.2124	Off	Out	$\delta p -3\%$
3700	Multi-C	23^0	2.600/2.2808	Off	Out	
3701	Multi-C	23^0	2.600/2.2808	On	Out	
4201-4205	Multi-C	25^0	2.505/2.1975	Off	In	

Table 2.3: Run list of optics data, where Dummy4cm means two dummy foils separated by 4 cm, and Multi-C means the optics target with seven carbon foils. Two HRSs took data simultaneously with the same settings.

The optics matrices used to replay optics calibration data were taken from previ-

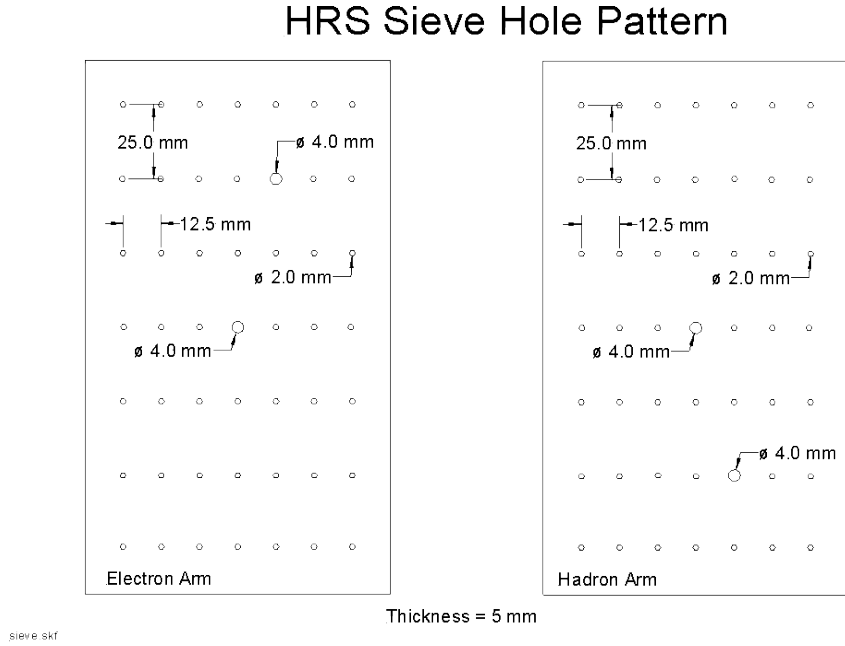


Figure 2.10: The design of sieve slit plates. Both arm have the identical plates but different mounting system. The graphic is taken from Hall A web-page.

ous experiments which shared similar spectrometer settings as this experiment. The initial HRS-L matrix taken from E05-102 experiment [19] was proved to be able to reconstruct the target plane quantities with good accuracy. The matrix was refitted by using the calibration data and the updated offsets from survey reports. The HRS-R optics matrix used by previous experiments, however, performed poor reconstruction of the target plane quantities because of the mis-tuning RQ3 field, as shown in Fig. 2.11a and Fig. 2.12a. The detailed procedure to calibrate the new HRS-R optics matrix will be discussed below.

On top of the old matrix elements, additional matrix elements were added in the optics terms to form a complete set of polynomials upto the *5th-order*, but the values of new elements were all set to zero. After the calibration data being replayed with this optics matrix, events selection on the focal plane was performed to select event from main trigger (T1). One-track cut on VDCs and PID cuts on the GC and calorimeters

were applied to select good scattered electrons. Events at the edge of HRS acceptance were eliminated by cutting the flat regions of the focal plane quantities.

Events from Run-3700 was used to calibrate the matrix elements in Y terms (Eq (2.9)). When one plots the 2-D histogram of z_{react} versus ϕ_{tg} (Fig. 2.11a), events scattered from a specific foil formed a strip, both ends of which were smeared due to the defocusing effect from RQ3. The first iteration was to select events near the center of each strip (the red boxes in Fig. 2.11a), and events in the overlap regions were discarded. The real value of z_{react} for each event was assigned with the position of the foil where the event belongs to. After the offsets in Table 2.1 and Table 2.2 being updated in the calibration, the matrix elements in Y terms were fitted by an optics optimizer based on the Minuit minimization method [20]. The high order elements in Y terms were generally removed before the minimization starts to fluctuate. The data was replayed with the new matrix elements updated in the database and the big improvement of z_{react} distribution is demonstrated in Fig. 2.11b.

The procedure of calibrating T terms and P terms was similar but used calibration data taken with a sieve slit plate (Run 4201~4205). The data were firstly replayed with new elements of Y terms. The sieve slit patterns shown in a 2-D plot of target plane quantities θ_{tg} and ϕ_{tg} were compared with the design of the sieve slit plate in Fig. 2.10. In the left plots of Fig. 2.10, each spot corresponds to the one sieve slit hole. For an event which could be clearly identified from a spot, the coordinate of this event on the sieve slit plane, (x_{ss}, y_{ss}) , was given as at the center of the hole since the diameter of the hole is tiny. The values of θ_{tg} and ϕ_{tg} can be directly calculated from the values x_{ss} and y_{ss} .

The matrix elements of T terms and P terms were fitted separately with the same optimizer and unnecessary matrix elements were carefully checked and removed. Fig. 2.12b shows that the sieve slit holes were well aligned after the calibration of angular terms.

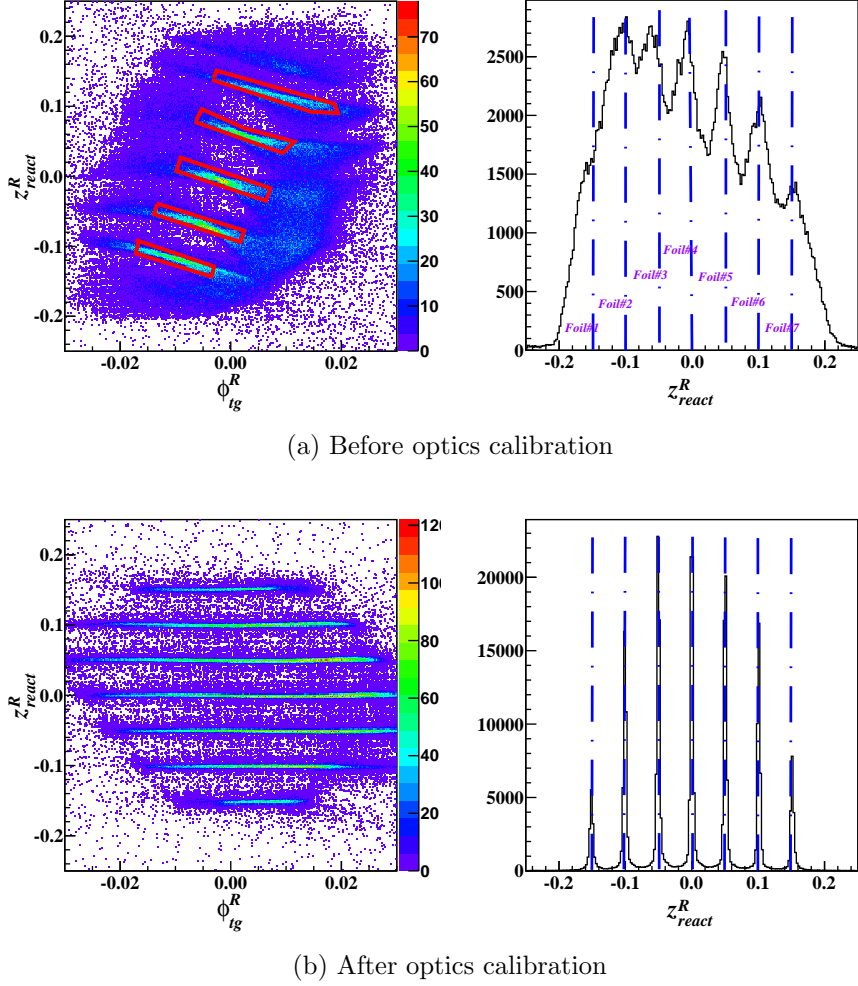


Figure 2.11: Z_{react} distribution before and after the optics calibration. The 2-D plots reveal that each strip represents electrons scattered from the corresponding foil indicated in the 1-D plots. The red boxes in the first 2-D plot represent graphic cuts applied to selected good electron samples during the first iteration of the Y terms calibration.

With updated Y terms, T terms and P terms in the data base, the calibration runs were replayed again, and the second iteration was proceeded with more good events included since the reconstruction of target plane quantities became much better. The calibration was completed when the fluctuation of the minimization began after several iterations.

The calibration of D terms requires the calibration data taken when the central momentum was intentionally shifted by small values, for example, off by $\pm 3\%$. However,

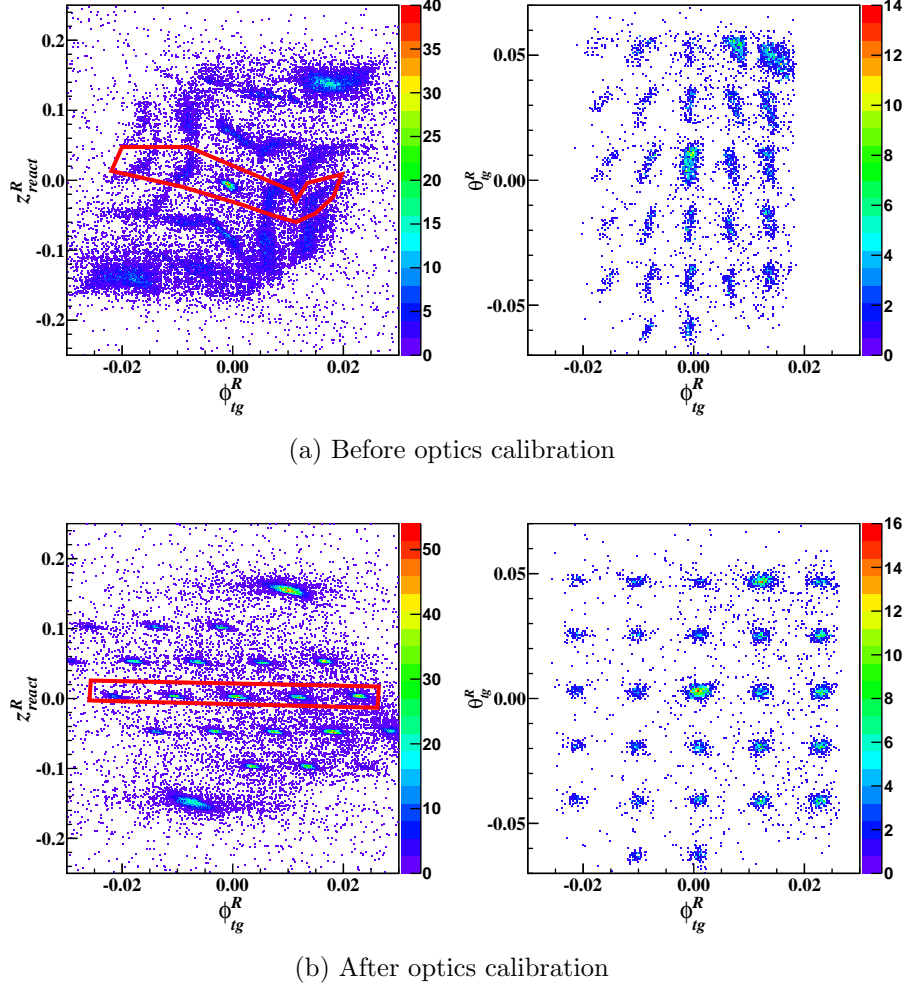


Figure 2.12: Z_{react} Sieve slit pattern before and after the optics calibration. Cutting on a single foil (the red box) is required to see the clear sieve slit pattern. Events from each hole are individually extracted and assigned with the values of θ_{tg} and ϕ_{tg} at the center of the hole.

the experiment was running at QE region and the peak of the momentum distribution was too broad to be sensitive to the small offsets. Without the elastic data, the D terms was unable to calibrated. In Appendix C, a different method was discussed to obtain the correct δp reconstruction.

Bibliography

- [1] J. Alcorn *et al.*, Nucl. Instrum. Meth. **A522**, 294 (2004).
- [2] B. Reitz, Hall-A BPM Calibration Procedure, <http://hallaweb.jlab.org/podd/doc/bpm.html>.
- [3] P. Solvignon-Slifer, E08-014 BCM calibration report, 2012.
- [4] P. V. J. Berthot, Nucl. Phys. News **9**, 12 (1990).
- [5] O. Ravel, 1997.
- [6] Jefferson lab cryogenic group, wwwold.jlab.org/eng/cryo.
- [7] D. Meekins, E08-014 target report, http://hallaweb.jlab.org/experiment/E08-014/analysis/HallA_Target_Configuration_Apr2011.pdf, 2011.
- [8] R. Bock and A. Vasilescu, The Particle Detector Brief ook.
- [9] E. Jastrzembski, 1997.
- [10] ROOT/C++ Analyzer for Hall A.
- [11] ROOT - A Data Analysis Framework by CERN, <http://root.cern.ch/drupal/>.
- [12] E08-014 Harp scan results, 2011.
- [13] A. Ketikyan *et al.*, About Shower Detector Software, 1997.
- [14] H. Lu *et al.*, Shower Calibration and Efficiency for E97-110, ShowerCalibrationandEfficiencyforE97-110, http://hallaweb.jlab.org/experiment/E97-110/tech/shower_calib.ps.gz", 2005.
- [15] N. Liyanage, Optics Calibration of the Hall A High Resolution Spectrometers using the new optimizer, <http://hallaweb.jlab.org/publications/Technotes/files/2002/02-012.pdf>, 2002.
- [16] Hall A survey report 1343, <http://www.jlab.org/eng/survalign/documents/dthalla/A1343.pdf>, 2010.

- [17] Hall A survey report A1249, <http://www.jlab.org/eng/survalign/documents/dthalla/A1239.pdf>, 2009.
- [18] Hall A survey report A1239, <http://www.jlab.org/eng/survalign/documents/dthalla/A1249.pdf>, 2009.
- [19] G. Jin, Measurement of the Target Single-Spin Asymmetry in Quasi-Elastic ^3He , 2011.
- [20] J. Huang, HRS Optics Optimizer, 2009.